SKA1 IMAGING SCIENCE PERFORMANCE

Document number .....SKA-TEL-SKO-DD-XXX
Revision.....REV A DRAFT 2
Author.....R.Braun
Date 2013-10-02
Status .....DRAFT

Name	Designation	Affiliation	Date	Signature
Additional Authors				
Approved for release:				

DOCUMENT HISTORY

Revision	Date Of Issue	Engineering Change Number	Comments
A	20130906	-	First draft.

DOCUMENT SOFTWARE

	Package	Version	Filename
Wordprocessor	MsWord	Word 2011	SKA1_Sys_Baseline_SysML(RevA_draft1).docx

ORGANISATION DETAILS

Name	SKA Program Development Office
Physical/Postal Address	SKA Organisation Jodrell Bank Observatory Lower Withington Macclesfield Cheshire SK11 9DL
Fax.	+44 (0)161 275 4049
Website	www.skatelescope.org

1 Abstract

In this memo we summarise the anticipated imaging science performance of the current SKA Phase 1 Baseline Design, including some minor configuration variants relative to what has previously been published.

2 Introduction

In March 2013, the "SKA1 System Baseline Design" (BD) document was published, representing a major milestone in terms of a well-specified concept for what would be deployed. While covering many aspects of the physical system, some additional work is still required to translate those specifications into performance figures under realistic observing scenarios. Here we attempt to provide that supplementary analysis in a self-consistent and easily accessible form.

3 Configurations

Nominal array configurations were discussed in the BD document for the SKA1–MID and –SUR facilities, while a very schematic configuration was presented there for –LOW. Unfortunately, there was little opportunity to undertake any science optimisation of those configurations given the time pressures of BD delivery. In the case of the –LOW configuration the situation is exacerbated by the fact that no constraint on minimum separation of the aperture array stations was imposed. This led to a design in which the majority of apparent stations within the highly concentrated core would physically overlap with one another, implying that it could never be successfully deployed. In fact, the BD requirement of providing the highest possible brightness sensitivity for –LOW leads to a configuration that is essentially completely filled at all radii up to about 600m. Such a tightly packed distribution of stations brings its own special challenges to configuration design, since there is almost no space available for the randomisation that would normally be used to improve visibility sampling. In this document we explore the first "second generation" SKA1 configurations. In all cases, we have maintained the basic distribution of collecting area with scale as presented in the BD and the existing ASKAP and MeerKAT dish locations, but have made an attempt to improve the range of angular scales over which good imaging performance and sensitivity are achieved. Moreover, we have respected the physical constraints of requiring non-overlapping station footprints as well as the large-scale geographic constraints that are currently thought likely to apply to –SUR and –LOW. No attempt has yet been made to employ realistic site masks. These will be used in the next iteration of configuration optimisation. The resulting configurations are illustrated in Figure 10 of Appendix A and are available digitally on request from the author. Only after suitable review will these or other configuration variants be incorporated into the Baseline Design.

For illustration purposes we contrast our new, "second generation" SKA1 configurations with those shown in the baseline design for –MID and –SUR, while for –LOW we contrast two variants that are both physically realisable. Both –LOW configurations we consider make use of "super-stations" beyond the central core. A super-station consists of 8 sub-stations deployed as a central sub-station surrounded by 7 others, all of 45m diameter. (The orientation of the set of 7 surrounding sub-stations is chosen randomly for each super-station.) In one case we deploy such close-packed super-stations throughout the core as well, while in the other case we deploy a close-packed set of discrete 45m sub-stations throughout the core. For both the "super-station" and "discrete" variants of the –

LOW configuration core, our imaging simulations employ correlations between all sub-stations in the entire array.

4 Observing Modes

The basic observing mode that is employed for an imaging experiment with an array of antennas or aperture array stations is a sky-tracking observation. Since the visibility sampling is improved with long duration tracks, we will consider the longest practical tracks consistent with good performance of the type of receptor being employed, namely 8 hour tracks that extend from – 4 h to + 4 h of Right Ascension for the dish arrays and 4 hour tracks, extending from – 2 h to + 2 h for the aperture arrays. While the character and quality of the visibility coverage is also influenced to some degree by the Declination of the field being observed, we will concentrate on the middle of the accessible Dec. range near – 30° as an illustrative example. Generally, the coverage will become even more symmetric and complete for more negative Declinations, while Declinations near 0 are the most limited.

Further, we will consider both “spectral line” and “continuum” observing modes, with “spectral line” providing essentially monochromatic visibilities, and with “continuum” being defined as constituting a 30% fractional bandwidth that is simulated with 30 spectral channels each of 1% width. Although many current facilities, as well as the planned SKA1, will achieve larger fractional bandwidths, there is the very practical issue of what exactly does it mean to have a source flux density that has been measured, for example, between 1 and 2 GHz? This is not a well-defined quantity, since the vast majority of real radio sources have a spectral energy distribution that changes very significantly across that total band, with some rising, some falling and others flat or even peaked. Two surveys, reaching the same apparent depth (expressed in Jy/beam), at the same centre frequency, but different total bandwidths would see very different source populations. “Sensitivity” across such large bands is clearly not a very useful concept, even without considering the associated complication of frequency dependent field-of-view. It should of course be considered that under many circumstances it will be possible to observe more than one of such continuum bands simultaneously and the greater this number, the greater the scientific utility in general.

5 Imaging Performance at a Nominal Frequency

The 8- and 4-hour sky-tracking observations (for dishes and stations) described above were simulated in the *miriad* package using the array configurations described above. The resulting monochromatic image quality and noise performance is shown in Figure 1, while the corresponding continuum performance, employing so-called multi-frequency synthesis is shown in Figure 2. A nominal centre frequency of 1.4 GHz was chosen for –MID and –SUR and 140 MHz for –LOW.

The RMS fluctuation levels were measured in simulated noise images measuring 2048x2048 pixels that employed an image cell size chosen to provide 4x4 pixels per FWHM sampling of the synthesized beam-width. The synthesized beam-width was adjusted by specifying uniform weighting of all measured visibilities, followed by application of a circular Gaussian tapering function. These RMS levels are normalised by the RMS noise level measured in a naturally weighted 2048x2048 image employing all measured visibilities.

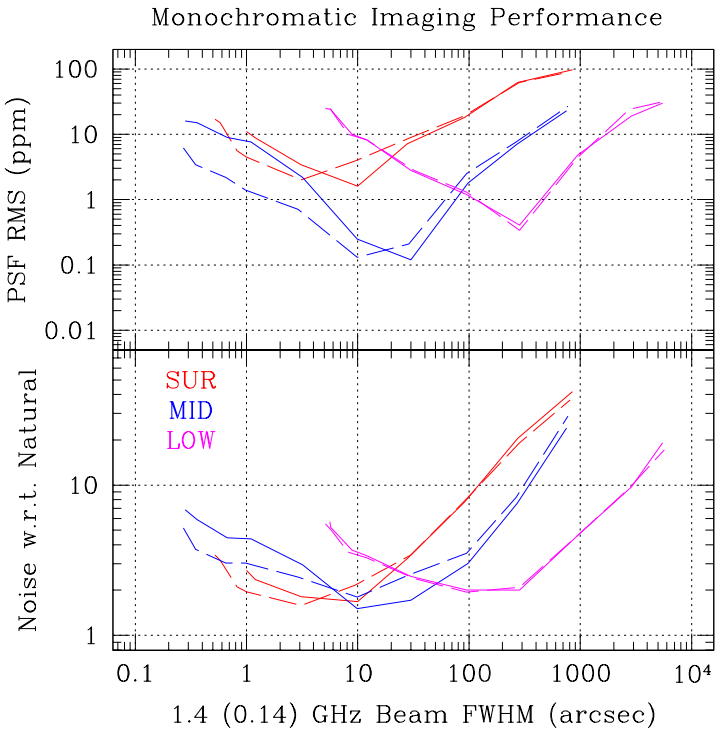

Figure 1. Monochromatic image noise and PSF quality performance of the SKA1 configurations as function of angular scale.

The quality of the corresponding synthesized point spread function was determined by measuring the RMS side-lobe fluctuation level of the dirty synthesized beam within the central 10x10 beam areas, after exclusion of the entire central beam lobe. As noted previously, a 4x4 pixel per achieved FWHM sampling was employed for these measurements. This measure emerged as providing the most relevant PSF quality estimator, at least from the perspective of distinguishing compact sources from one another or estimating partially resolved source attributes. The RMS level is expressed in "parts per thousand (mille)". Another complementary PSF quality estimator is the far side-lobe fluctuation level, which will be of particular importance for high dynamic range calibration. In practise it was found that these two PSF indicators are not correlated with each other. They are tied to very different aspects of the visibility sampling.

Solid lines show the BD configuration performance for –MID and –SUR, while the long-dashed lines are the corresponding "second generation" configurations. The new configurations were intended to broaden out the "sweet spot" of performance, defined in terms of both the relative array sensitivity and PSF quality. As noted above, the two –LOW configurations being contrasted are both physically realistic and differ only in whether they employ the "super-station" or "discrete" sub-station concept within the core. In fact, there are no significant performance differences between these two variants of –LOW.

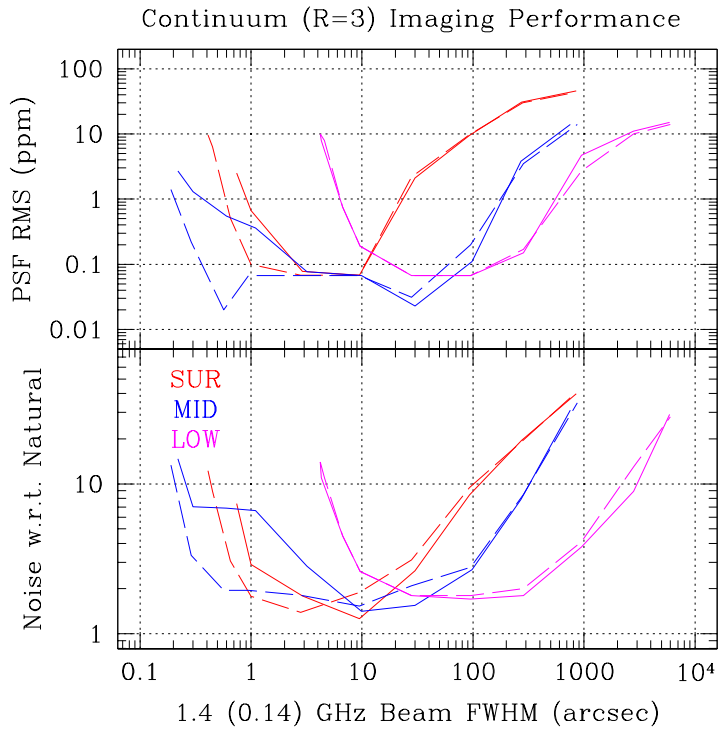

Figure 2. Continuum mode noise and PSF performance of the SKA1 configurations as function of angular scale.

The corresponding performance in continuum mode is shown in Figure 2. The multi-frequency synthesis provides a significant broadening of the performance "sweet spot" to encompass a much broader degree of angular scales relative to the monochromatic case. The PSF quality has improved by more than an order of magnitude over the spectral line case. The enhanced noise and PSF performance of the new –MID configuration at high angular resolution is quite apparent.

6 Survey Performance

Having established the impact of the configuration on noise performance as a function of scale at some reference frequency, it is possible to calculate the performance of specific observing campaigns as a function of both centre frequency and angular scale. At any fixed frequency we can simply rescale the beam dimension from our nominal measurements (Figures 1 and 2) since it corresponds to the same antenna configuration relative to another observing wavelength. The absolute sensitivity of each configuration at a specific frequency is given by the relevant System Equivalent Flux Density (SEFD). The SEFD as function of frequency for each of –LOW, –MID, and –SUR, including the planned receiver coverage of the MeerKAT antennas and a single SKA PAF band deployed in the ASKAP dishes, is taken directly from the BD and is summarized in Appendix B for easy reference. Since we apply the same performance versus scale template as shown in Figures 1 and 2 to all frequencies (albeit with suitable wavelength scaling), we make a small error for those frequency ranges where the ASKAP or MeerKAT antennas are not equipped with receivers that overlap with the new SKA bands (see Appendix B), since they will not then contribute to the visibility coverage. We make use of "second generation" configurations throughout.

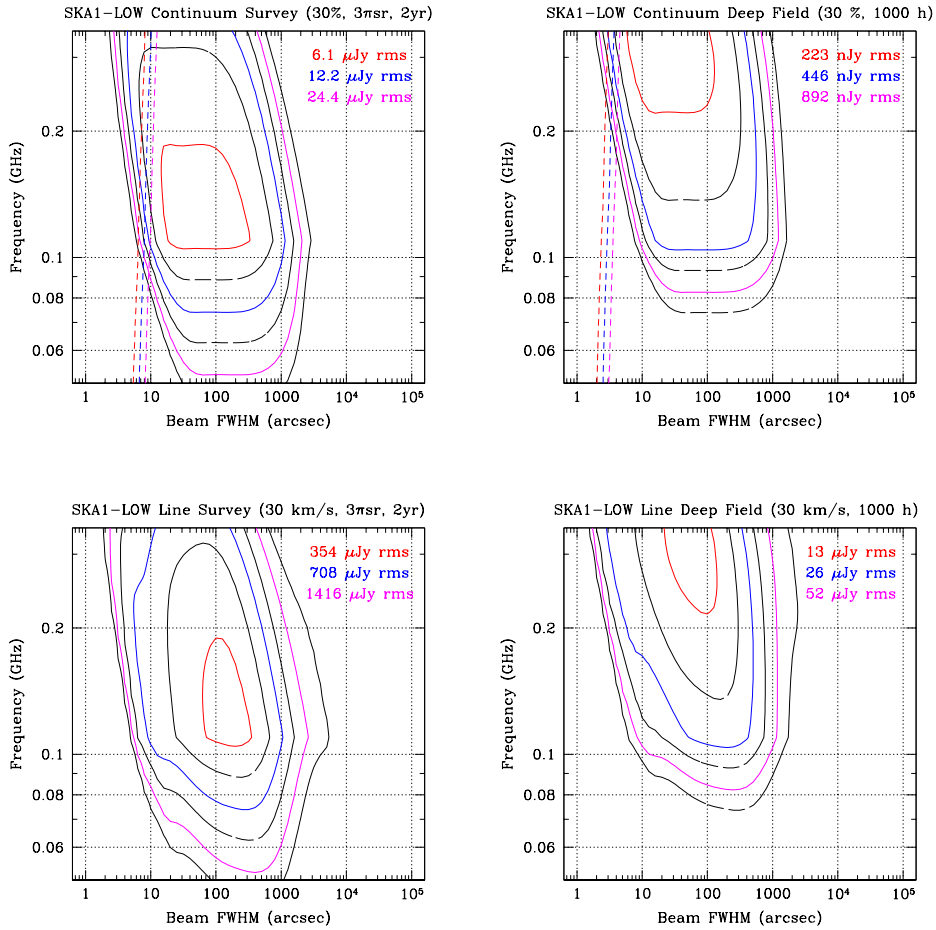

Figure 3. The all-sky and deep-field sensitivity performance of SKA1-LOW as function of angular scale and centre frequency. Source confusion levels for continuum observations are also indicated by the diagonal contours.

For simplicity we begin by considering only two extreme observing scenarios that are likely to encompass the full range of actual observations. The first is an “all-sky” survey that provides 3π sr coverage with a 2 year net total integration time. In this case, the instantaneous FoV of each antenna system at each centre frequency is used to calculate the fraction of two years integration that is available for each field. The second scenario involves undertaking a single “deep-field” observation of 1000 hours net integration time. In this case, the field-of-view that is provided is quite different for each facility and each centre frequency (see Appendix B). From this starting point it is straightforward to rescale (by square root integration time) one of these two outcomes to reflect any other observing strategy targeting other survey areas or depths.

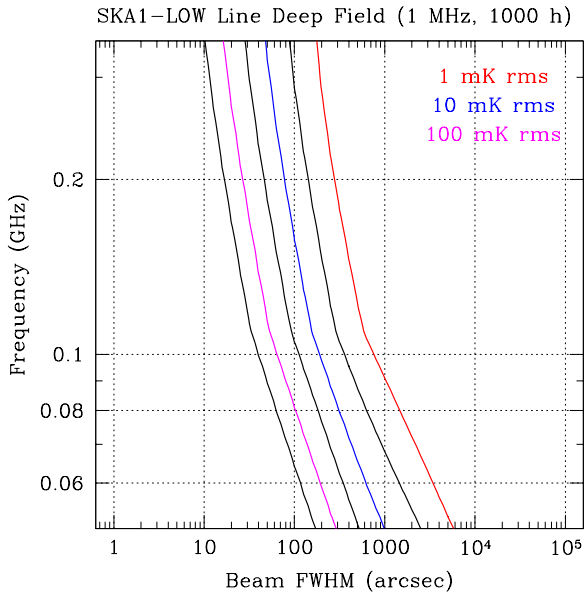

Figure 4. The noise performance of a deep spectral-line observation with SKA1-LOW expressed in brightness temperature units.

We consider both the spectral line and continuum thermal noise performance characteristics, where "continuum" is again defined as implying a 30% relative bandwidth, while spectral line is defined by a narrower bandwidth which varies somewhat according to the specific application and is clearly labelled in each plot. Some of the relevant choices are a fixed velocity width of either 30 or 100 km/s at each observing frequency (to represent resolved imaging or unresolved galaxy detection experiments respectively), or 1 MHz channel bandwidth for a deep-field –LOW observation. The likely confusion noise level of continuum observations is indicated by the coloured diagonal short-dashed contours following the parameterised model presented by Condon et al. 2012 (ApJ 758, 23). Higher levels of confusion noise occur to the right of each labelled contour. We also express the spectral-line noise performance for a deep field observation in units of brightness temperature. Lower brightness temperature RMS is found to the right of each labelled contour.

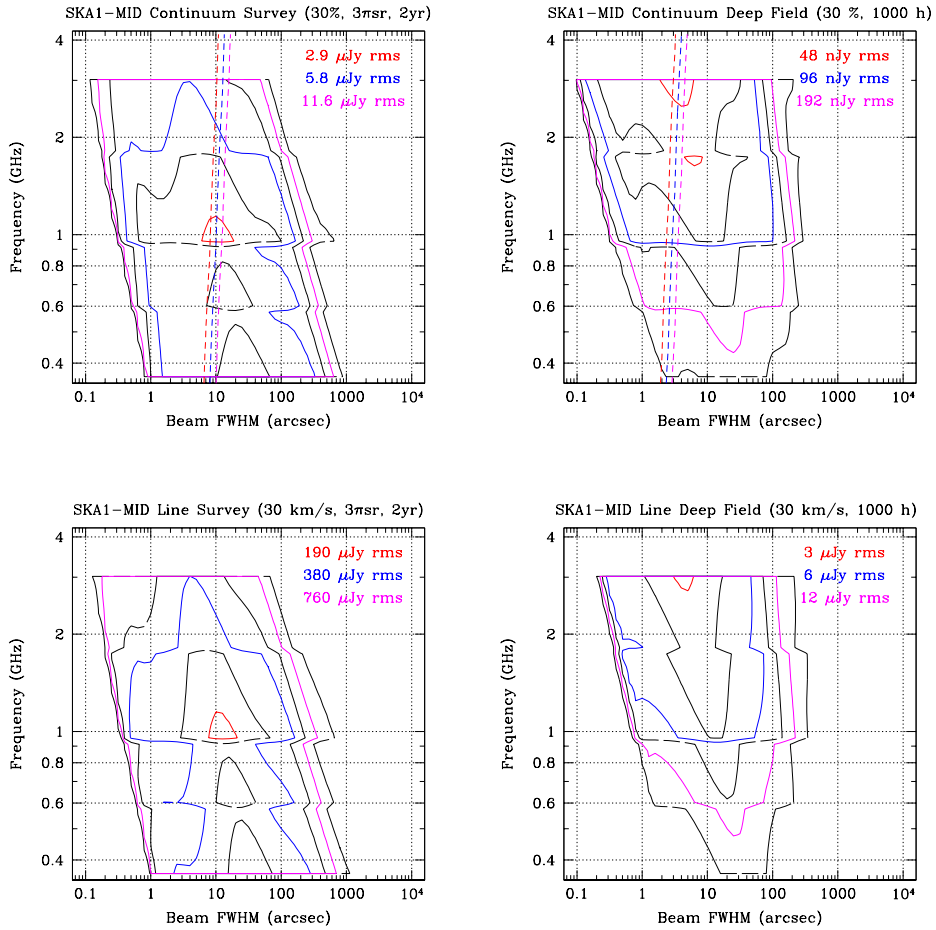

Figure 5. The all-sky and deep-field sensitivity performance of SKA1-MID as function of angular scale and centre frequency. Source confusion levels for continuum observations are also indicated by the diagonal contours.

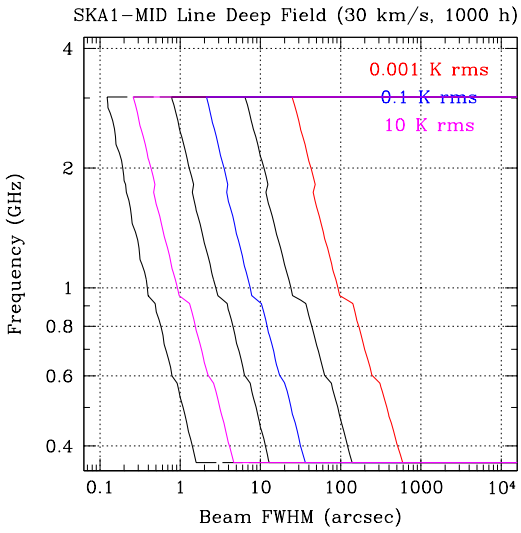

Figure 6. The noise performance of a deep spectral-line observation with SKA1-MID expressed in brightness temperature units.

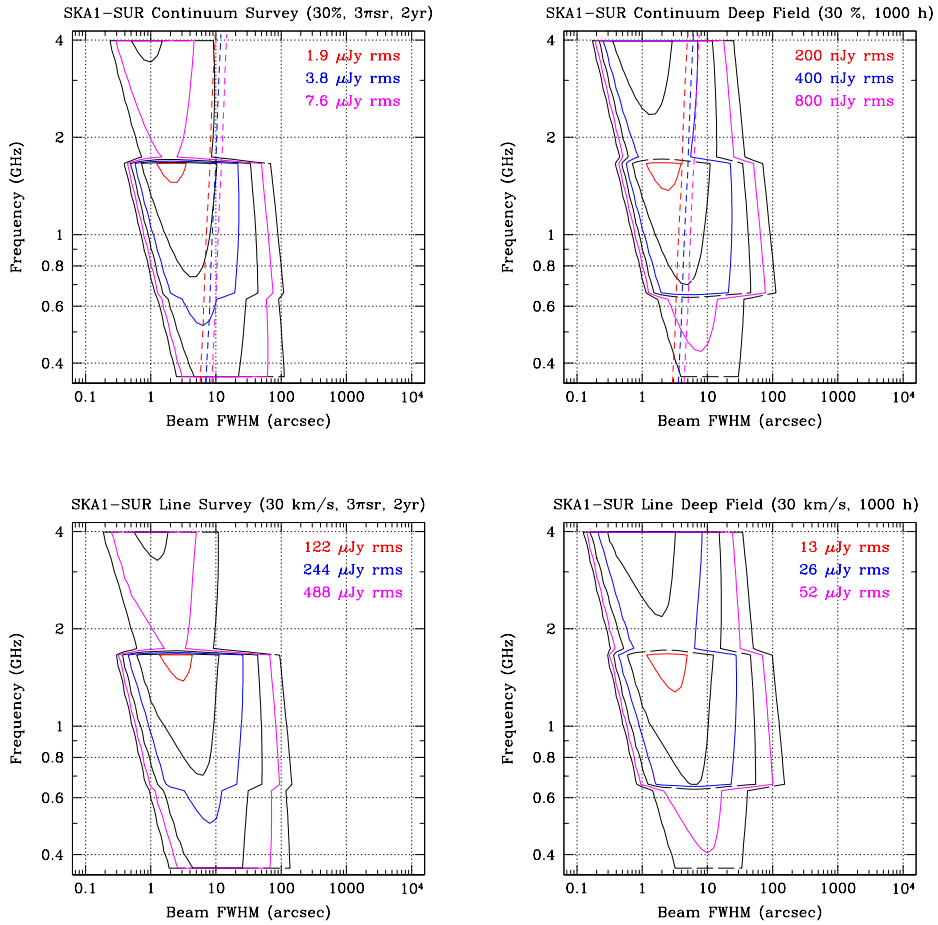

Figure 7. The all-sky and deep-field sensitivity performance of SKA1-SUR as function of angular scale and centre frequency. Source confusion levels for continuum observations are also indicated by the diagonal contours.

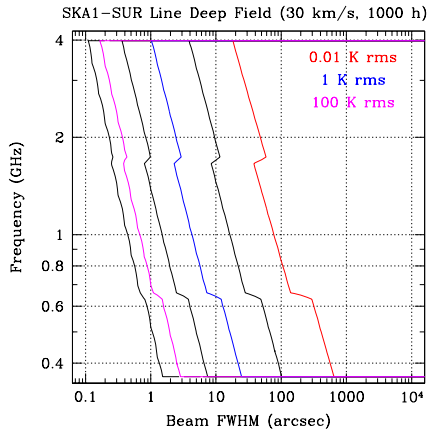

Figure 8. The noise performance of a deep spectral-line observation with SKA1–SUR expressed in brightness temperature units.

Next we include plots that show the 5σ spectral-line sensitivity levels of –SUR and –MID expressed in units of solar masses of neutral hydrogen as traced by optically thin, red-shifted 21cm emission assuming H_0 = 67.3 km/s and Ω_m = 0.32 (Ade et al. 2013arXiv1303.5076P) for calculation of the relevant luminosity distance. Three nominal levels are labelled in each plot $\log(M_\odot)$ = 8.5, 9.5 and 10.5, that correspond to typical HI masses of dwarf, M_{HI}* and ultra-gas-rich systems in the local Universe.

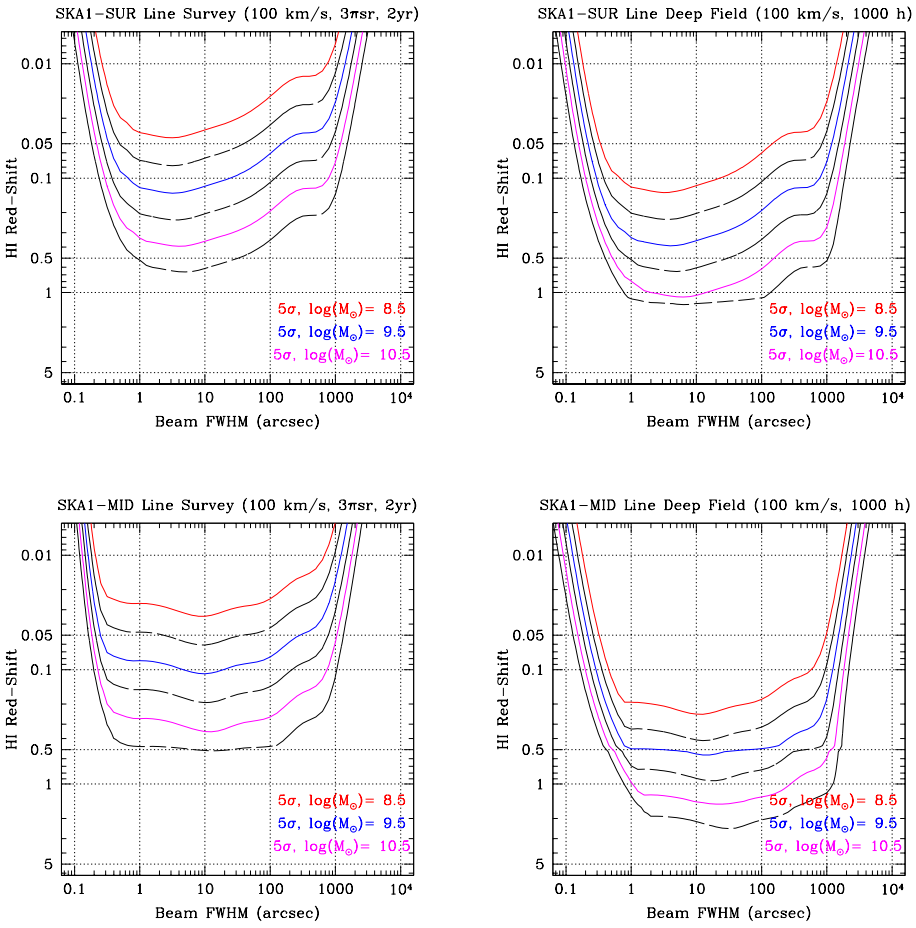

Figure 9. The all-sky and deep-field spectral-line survey performance of SKA1–SUR and –MID expressed as the mass of neutral hydrogen traced by red-shifted 21cm emission as function of angular scale.

It is also interesting to consider the total number of 21cm detections of galaxies that might be achieved with particular surveys. For simplicity, we will assume that a representative line-width for galaxy detection is 100 km/s. Narrower intrinsic line-widths would have somewhat higher signal-to-noise, while wider line-widths slightly reduced signal-to-noise with respect to this nominal assumption. In practise, previous authors have found that number counts based on this simple premise are quite accurate relative to more complex models that account for an assumed line-width distribution.

The number of galaxy detections, above some limiting mass, M_T, at some redshift, can be calculated by integrating the HI mass function (HIMF) above that mass within the volume defined by the redshift bin and the survey solid angle, Ω_{SUR}, on the sky. The parameters describing the local universe

HIMF have recently been estimated by Martin et al. (2010, ApJ 723, 1359) to be a space density of ϕ_* (h^3_{70} Mpc^{-3} dex^{-1}) = 4.8 10^{-3} +/- 0.3, a characteristic mass log ($M_*/M_\odot$) + 2 log(h_{70}) = 0.96 +/- 0.02 and a faint end slope of α = -1.33 +/- 0.02. While the redshift evolution of the HIMF is not yet determined and is one of the obvious goals of an actual survey, there is a well-documented evolution in the volume density of HI from the SDSS Damped Lyman Alpha absorption statistics, that increases to about twice its current value by $z \approx 4$ (Noterdaeme et al. 2009, A&A 505, 1087). How that increase might be split between number and mass evolution is not known, but if one assumes for example only mass evolution it might be described as $\log(M_*(z)) = \log(M_*)_{z=0} + 0.075\ z$. The number of detected galaxies is then:

$$N(M_{HI}>M_T,\ z) = \Sigma_{Mt \rightarrow Mx}\ V(z)\ d\log(M_{HI})\ \ln(10)\ \phi_*(M_{HI}/M_*(z))^{\alpha+1}\ \exp(-M_{HI}/M_*(z)),$$

with $V(z) = \Omega_{SUR}\ (D_{C+}{}^3 - D_{C-}{}^3)/3$, and the co-moving distance at the far, D_{C+}, and near, D_{C-}, edge of each redshift bin is as specified in Appendix B and $d\log(M_{HI})$, the logarithmic increment in M_{HI} over which the mass function integral is being calculated through some maximum HI mass, M_x. The galaxy number per redshift interval is given by summation over the chosen interval of redshift bins. For example, the plots below are calculated per logarithmic redshift interval of 0.3 dex.

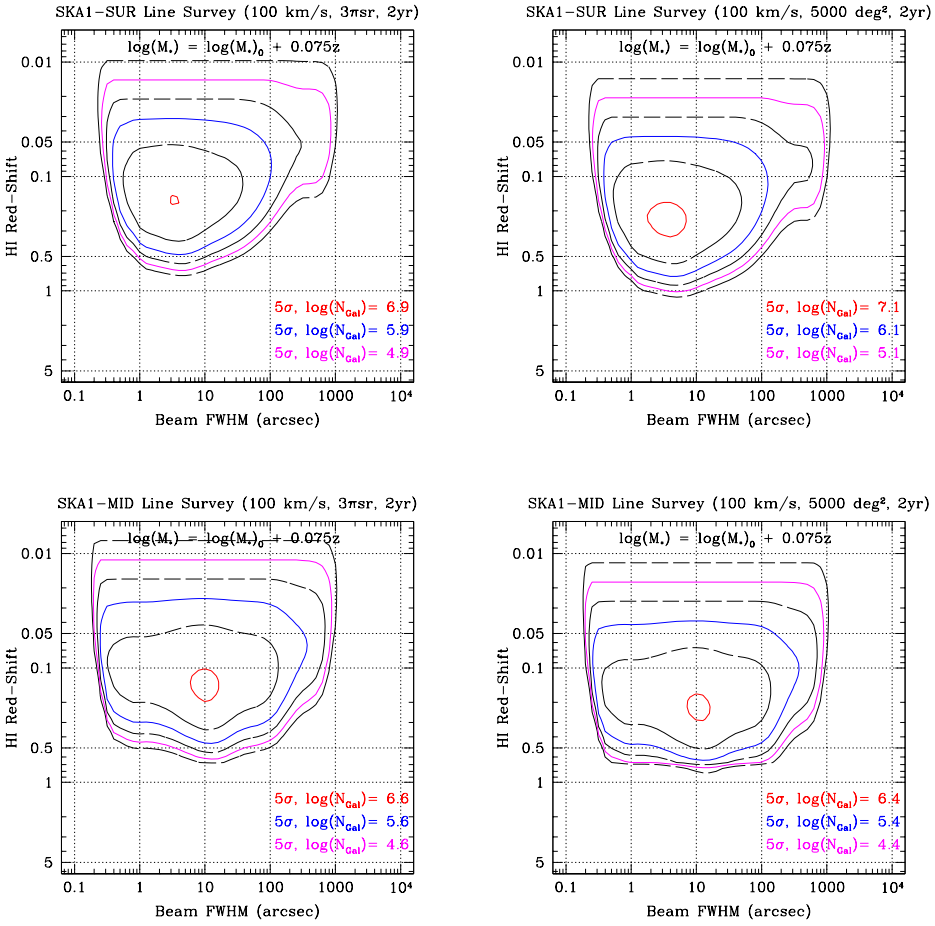

Figure 10. The all-sky and wide-field spectral-line survey performance of SKA1–SUR and –MID expressed as 5σ detection numbers of unresolved galaxies per 0.3 dex of log(z) as traced by red-shifted 21cm emission as function of angular scale.

Appendix A. "Second Generation" Configurations

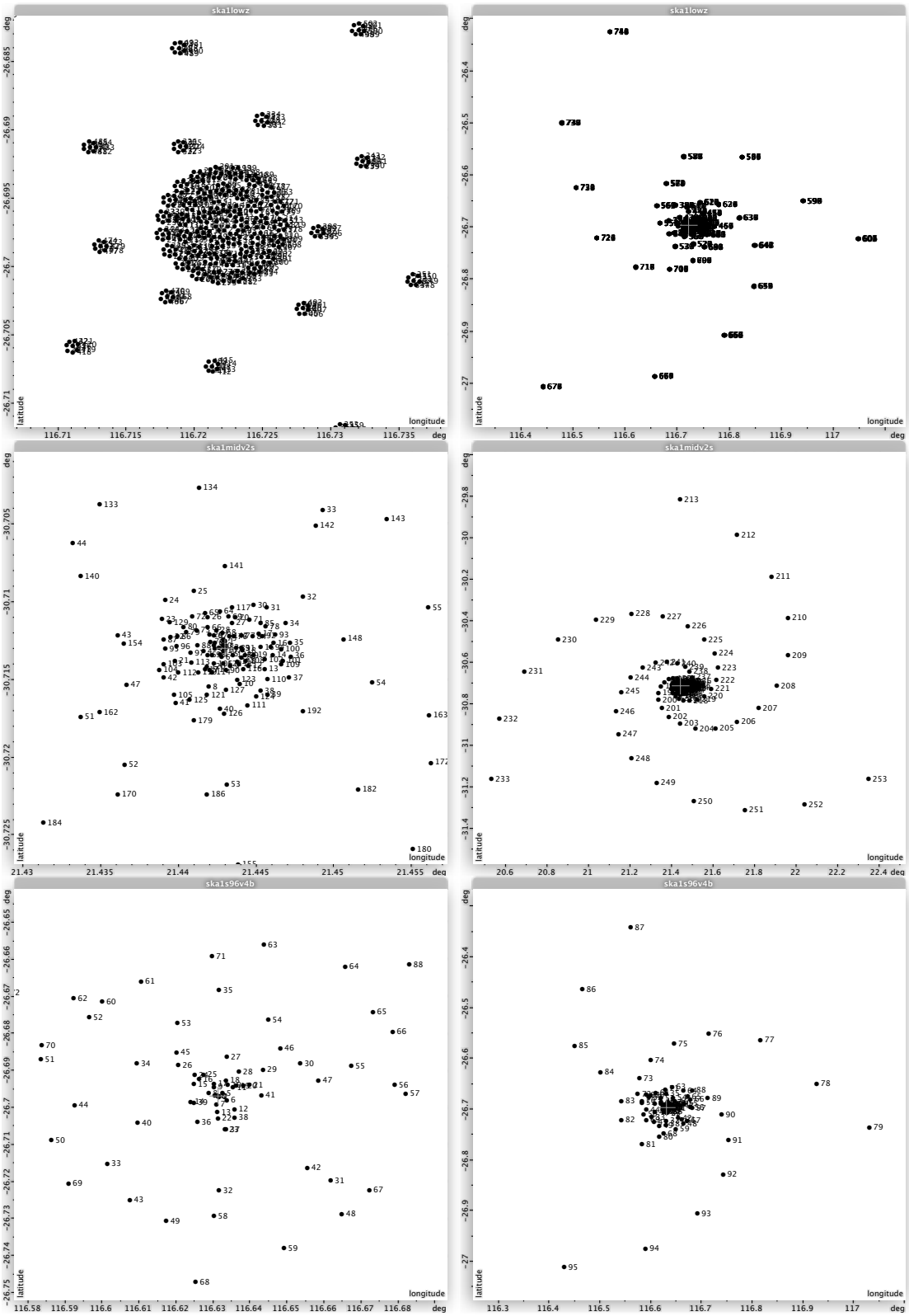

Figure 11. The core (left) and remote (right) configurations of SKA1-LOW (top), -MID (middle) and -SUR (bottom) that have been used for performance calculations.

Appendix B. Background Notes for Performance Calculations

General Relationships

Effective $FoV_{beam} = (\pi/8)(1.3\lambda/d_{ant/station})^2$, since noise equivalent area involves squared beam.

$SEFD = 2k_BT_{sys}/A_e$ for an individual antenna.

$SEFD_{array} = 2k_BT_{sys}/ A_e$ for the total of all antennas.

$SEFD_{array}=1/(n/SEFD_{ASKAP} + m/SEFD_{SKA})$, where SEFDs are the n ASKAP and m SKA antennas, respectively.

$S_{RMS} = SEFD_{array}/(\eta_s(2\Delta\nu\ \tau)^{1/2})$, where η_s is the system efficiency, $\Delta\nu$ is the channel bandwidth, and τ is the total integration time. η_s is taken as 0.9.

$T_{RMS} = (\lambda^2/2k_B)(S_{RMS}/\Omega_{array})$.

$\Omega_{array} = (\pi/4)(1.3\lambda/B_{eff})^2$ in terms of some effective baseline, B_{eff}.

$M_{HI}/(M_\odot) \approx 49.8\ S_{TOT}/\ (Jy\ Hz)\ [D_L\ /(Mpc)]^2$ (eg. Duffy et al 2012, MNRAS 426, 3385)

$S_{TOT} = S_\nu\ \Delta\nu$

$D_L = D_C\ (1+z)$ is the luminosity distance in terms of the co-moving distance, D_C.

$D_C \approx D_H\ z\ /\ (1 + 1.718\ \Omega_m\ z + 0.315\ \Omega_m^{\ 0.5}\ z^2)^{\ 0.5}$

(eg. Lampton 2010, www.ssl.berkeley.edu/~mlampton/ComovingDistance.pdf),

and the Hubble distance, $D_H = c\ /\ H_0$.

SKA1-SUR

PAFs:

Bands: 0.35 – 0.9, 0.65 – 1.67, 1.5 – 4.0 GHz

Band centres: 0.63, 1.2, 2.8 GHz

Effective FoV of one beam @ band centre: 1.75, 0.5, 0.090 deg^2.

Effective PAF FoV: 63, 18, 3.25 deg^2.

SEFD per SKA Dish in Bands 1, 2, 3: 976, 586, 781 Jy

SEFD per ASKAP Dish in Band 2 only: 915 Jy

Total SEFD of 60xSKA plus 36xASKAP: 16, 7.1, 13 Jy

Sensitivity as A_e/T_{sys}: 173, 391, 212 m^2/K

SKA1-MID

SPFs:

Bands 1a/b, 2 and 3: 0.35 – 1.05, 0.95 – 1.76, 1.65 – 3.05 GHz

Band centres: 0.7, 1.4, 2.4 GHz

Effective FoV of one beam @ band centre: 1.4, 0.375 0.125 deg^2

SEFD per SKA Dish: 673, 400, 400 Jy

SEFD of 190 SKA Dishes: 3.5, 2.1, 2.1 Jy

MeerKAT Bands 1b and 2: 0.58 – 1.02, 0.9 – 1.67 GHz

MeerKAT SEFD per Dish: 831, 551 Jy

MeerKAT SEFD of 64 Dishes: 13, 8.6 Jy

Total SEFD of 190xSKA plus 64xMeerKAT: 3.5/2.8, 1.7, 2.1 Jy

Sensitivity as A_e/T_{sys}: 789/986, 1620, 1300 m^2/K

SKA1-LOW

$T_{rcvr} = 0.1T_{sky} + 40$ K

$T_{sys} = T_{rcvr} + T_{sky}$, where $T_{sky} = 60\lambda^{2.55}$.

Effective $FoV_{beam} = (\pi/8)(1.3\lambda/d_{station})^2$, since noise equivalent area involves squared beam.

$A_e = (\lambda^2/4\pi)\eta D$, where A_e is the element effective area, η is the radiation efficiency, and D is the directivity. This formula applies only to frequencies above the dense-sparse transition. For droopy dipoles η = 0.9 and D = 6.6 dBi, independent of frequency in the sparse region, equivalent to $A_e = \lambda^2/3.0$.

BD has η = 0.85 at 50 MHz and 0.99 at 300 MHz and an assumed D = 8 dBi

SEFD of full array @ 50, 110, 160, 220 MHz: 19, 2.9, 2.6 2.6 Jy

45m Station Effective FoV @ 50, 110, 160, 220 MHz: 39, 8, 3.8, 2.0 deg^2